ISA Transactions xxx (xxxx) xxx

Contents lists available at ScienceDirect

ISA Transactions

journal homepage: www.elsevier.com/locate/isatrans

Research article

Robust cascade controller for the power factor of the three-phase supply and the induction motor velocity

Onofre A Morfin [a,*], Riemann Ruiz-Cruz [b]
Fredy A Valenzuela [c], Reymundo Ramirez-Betancour [c]
Carlos E Castañeda [d], Fernando Ornelas-Tellez [e]

[a] Depto. de Electrica y Computacion, Instituto de Ingenieria y Tecnologia, Universidad Autonoma de Ciudad Juarez, Mexico
[b] Laboratorio de Investigacion en Diseño Optimo, Dispositivos y Materiales Avanzados (OPTIMA), Depto. de Matematicas y Fisica, ITESO, Tlaquepaque, Mexico
[c] Division Academica de Ingenieria y Arquitectura, Universidad Juarez Autonoma de Tabasco, Cunduacan, Mexico
[d] Centro Universitario de los Lagos de la Universidad de Guadalajara, Jalisco, Mexico
[e] Facultad de Ingenieria Electrica, Universidad Michoacana de San Nicolas de Hidalgo, Morelia, Mexico

ARTICLE INFO

Article history:
Received 25 January 2021
Received in revised form 18 May 2023
Accepted 9 June 2023
Available online xxxx

Keywords:
Controllable rectifier
Power factor
Reactive power controller
Motor speed controller
Induction motor

ABSTRACT

It is well known that induction motors consume active and reactive energy from the utility grid to operate; additionally, when a power converter drives the motor, a high content of current harmonics is produced, and both circumstances decrease the utility grid power factor, which later requires to be improved. To this end, this paper presents a novel complete solution through a robust control system employed in a back-to-back topology power converter to deliver, instead of consuming, regulated reactive power toward the main grid, which comes from a capacitor bank in a DC-bus. This salient feature of delivering reactive power, and simultaneously, regulating the speed for an induction motor, becomes one of the contributions of this work to enhance the power factor. The robust converter controller is synthesized in a cascade form, by applying the linearization block control and state-feedback techniques. These techniques are combined with the super-twisting strategy for canceling the nonlinearities and the effect of the external disturbances. The complete system consists of a back-to-back converter, an LCL filter coupled to the main grid for mitigating the current harmonic content, and an induction motor under variable load conditions. Experimental tests expose the performance and robustness of the proposed controller, where a robust control for the reactive power acts under sudden changes in the active power produced through abrupt variations in the motor load.

1. Introduction

The squirrel cage induction motor has been adopted for most drive units in industrial applications because of its simple structure and ruggedness. However, the design of the speed controller applied to this motor is very complex because of the mathematical model nonlinearities, strongly coupled dynamics, and time-varying parameters. In addition, the induction motor is known for worsening the power factor and diminishing the efficiency when its load factor is reduced. Whether the motor speed is controlled through an electronic drive to feed the stator winding, an AC/DC/AC converter is typically used with a non-controllable rectifier. The nonlinear characteristic of this converter affects the power quality in the utility grid, such as high content of current harmonics and low power factor value.

Some researchers have evaluated the controlled rectifier impact on the utility grid power quality improvement. In [1], a controller without a current sensor for regulating the DC bus voltage of a rectifier is proposed. The proposed controller keeps the DC bus voltage level at a reference value and unitary power factor, operating under nominal conditions and in the presence of voltage variations even. The controller is based on a unique proportional–integral control loop on *abc* system, and it does not require state observers or signal estimation. The controller is implemented through the sinusoidal pulse-width modulation technique, with a total harmonic current distortion of less than 5%. Nevertheless, a lower total harmonic current distortion could

* Corresponding author.
E-mail addresses: omorfin@uacj.mx (O.A. Morfin), riemannruiz@iteso.mx (R. Ruiz-Cruz), fredy.valenzuela@ujat.mx (F.A. Valenzuela), reymundo.ramirez@ujat.mx (R. Ramirez-Betancour), carlose.castanedah@academicos.udg.mx (C.E. Castañeda), fornelas@umich.mx (F. Ornelas-Tellez).

https://doi.org/10.1016/j.isatra.2023.06.009
0019-0578/

be obtained using a space vector pulse width modulation technique. In [2], an H^∞ control technique combined with a second-order sliding modes algorithm is proposed for controlling the real and reactive power in two-level three-phase power converters. Simulation tests are carried out considering linear loads and the results show a good performance near to the unity power factor, with a THD close to 0.46%. In [3], a Backstepping control methodology is presented in the direct power regulation for a 3-phase controlled rectifier by regulating the active and reactive power. The Backstepping algorithm is synthesized according to a split dynamic model for regulating the DC bus voltage and active/reactive power. This controller incorporates state observers based on a control set–model predictive control mechanism and is able of regulating instantaneous reactive power achieving that the current is in phase with the voltage, while kipping the DC bus voltage in its desired reference value, and the THCD is maintained around 2%. In that sense, in [4] a second-order sliding modes nonlinear observer with variable gain is applied to a three-level three-phase converter. The active and reactive power are controlled in the utility grid. The experimental and simulation results show a great performance even in presence of measurement noise and disturbances such as load variations. However, the experimental tests presented in both [3,4] do not consider non-linear loads, which could affect the current distortion value.

[5,6] present a control strategy to regulate the induction motor speed by optimizing the magnetic flux and keeping the unity utility grid power factor. The proposed methodology considers the magnetic saturation effect, meanwhile, the power converter is represented by an averaged model. The control design is based on an adaptive nonlinear multivariable controller. However, in that proposal, a single-phase controlled rectifier is applied instead of a three-phase controlled rectifier, which is a limitation in higher power industrial applications. In the same way, [7] addresses the induction motor speed control problem that considers the converter-machine model, including the magnetic saturation effect. The control strategy incorporates an optimizing reference function for regulating the squared flux modulus of the rotor winding, while the load torque and motor speed are estimated by an adaptive observer so that no mechanical sensors are required. There, an adaptive nonlinear feedback controller is applied for regulating the induction motor speed. The exposed results show a robust speed control, however, the power factor regulation is not addressed. Similarly, [8] develops an adaptive controller combined with the sliding-modes strategy to regulate the induction motor speed, where the motor is synthesized through the vector control technique, and it is described by a first-order system at a given operating point. The results of this proposal present a good accuracy and an effective response to the speed tracking, however, the chattering effect is presented in the controlled variables. Additionally, [9] presents an algorithm for improving the effectiveness of speed control of an induction motor. The controller design is based on the classical proportional–integral strategy combined with the Backstepping control technique to regulate the rotor flux against the load torque variations for minimizing the total power losses in the motor. Another rotor flux and speed controller that use the nonlinear Backstepping technique is presented in [10], where the mechanical sensor is not required, instead, the rotor speed is estimated through a speed observer. However, neither [9] nor [10] address the utility grid power factor regulation. It is worth mentioning that the revised literature does not present, to the best of our knowledge, the induction motor speed regulation with the characteristic of delivering reactive power toward the electrical grid.

This work proposes a novel complete solution for delivering regulated reactive power to the utility grid, and simultaneously, controlling the induction motor speed. This is achieved by using a cascade robust control system applied to an AC/DC/AC power converter. Then, the main contributions are: *(a)* to deliver regulated reactive power for contributing to the power factor improvement of the utility grid, *(b)* simultaneously, to regulate the induction motor speed through a robust control system under external disturbances, such as sudden variations in load torque. The above contributions are validated through experimental tests, which show the robustness and effectiveness of the controller proposal.

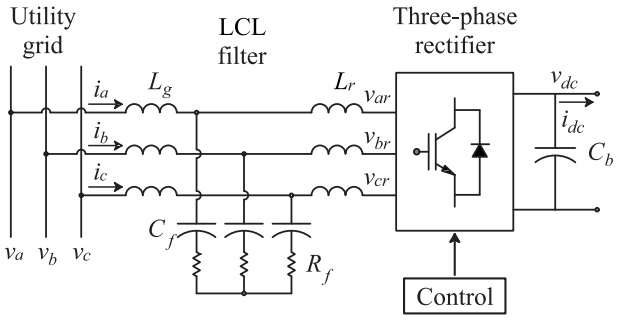

Fig. 1. Controlled rectifier system scheme.

The work developed in this paper is presented as follows. Section 2 describes the design process of the reactive power controller based on the controlled rectifier mathematical model. In Section 3, the process to obtain the induction motor model is detailed thoroughly. Section 4 presents the controller synthesis for regulating the induction motor speed and a differentiator for estimating the time derivative of the speed error; furthermore, a robust observer is designed to estimate the flux linkages of the rotor winding. Section 5 presents the controller performance through experimental results. Finally, the conclusions are shown in Section 6.

2. Control system for the reactive power regulation

The control scheme delivers regulated reactive power to the electrical grid, which contributes to the power factor enhancement, which directly influence on the overall utility grid performance. In particular, this system consists of the utility grid in connection with an LCL filter, a controlled rectifier-type bridge, and a capacitor bank located at a DC-bus, see Fig. 1. The reactive power comes from the capacitor element that is grid-connected through the controlled rectifier, where its corresponding control mechanism allows regulating the power to a reference value, which contributes to enhancing the power factor. Simultaneously, the rectifier controller is used for controlling the DC bus voltage.

2.1. Controlled rectifier model

The model of the controlled rectifier system is stated by considering, firstly, that the input-power from the electrical grid is equal to the bridge rectifier DC output-power, by neglecting the losses in both, the controlled rectifier and in the LCL-filter; secondly, by applying the voltage balance at the LCL filter terminals without considering the effect of the capacitor C_f to reduce the model order. Therefore, the model of the controlled rectifier becomes:

$$\begin{aligned} \mathbf{v}_{\mathrm{abc}}^{\top}\mathbf{i}_{\mathrm{abc}} &= v_{\mathrm{dc}}C_{\mathrm{b}}\frac{d}{dt}v_{\mathrm{dc}} + v_{\mathrm{dc}}i_{\mathrm{dc}} \\ \mathbf{v}_{\mathrm{abc}} &= \mathbf{v}_{\mathrm{abcr}} + R_{\mathrm{eq}}\mathbf{i}_{\mathrm{abc}} + L_{\mathrm{eq}}\frac{d}{dt}\mathbf{i}_{\mathrm{abc}} \end{aligned} \tag{1}$$

where $\mathbf{v}_{\mathrm{abc}}$ and $\mathbf{i}_{\mathrm{abc}}$ are the voltage and current vectors of the main grid; v_{dc} represents the DC bus voltage; $\mathbf{v}_{\mathrm{abcr}}$ is the rectifier input

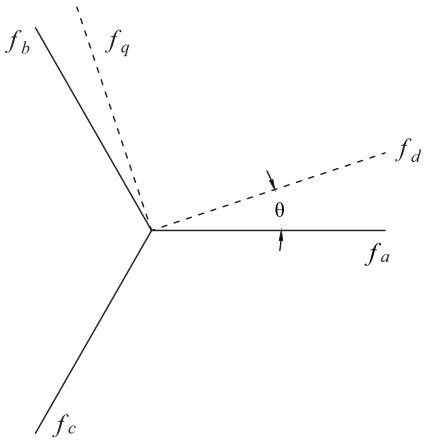

Fig. 2. *dq* axes representation.

voltage vector; i_{dc} becomes the DC current toward the controlled rectifier output; the capacitor C_b is connected in the DC-bus; R_{eq} represents the total resistance, and L_{eq} is the total inductance of the two coils of the LCL filter, neglecting the shunt branch constituted by the capacitor in series with the damping resistor.

It is a common practice to refer model (1) from *abc* to *dq* coordinate frame, that rotates at the utility grid frequency, with the aim of obtaining a decoupled model, where the voltages and currents become time invariant signals in steady state. The model in *dq* frame is achieved by applying the following similitude transformation, named Park transformation, whose graphic representation is pictured in Fig. 2, [11].

$$\mathbf{T}_s = \frac{2}{3}\begin{bmatrix} \cos\theta_s & \cos\left(\theta_s - \frac{2\pi}{3}\right) & \cos\left(\theta_s + \frac{2\pi}{3}\right) \\ -\sin\theta_s & -\sin\left(\theta_s - \frac{2\pi}{3}\right) & -\sin\left(\theta_s + \frac{2\pi}{3}\right) \\ \frac{\sqrt{2}}{2} & \frac{\sqrt{2}}{2} & \frac{\sqrt{2}}{2} \end{bmatrix} \tag{2}$$

The utility grid voltages are referred from the *abc* to *dq* by applying the Park transformation (2) as follows:

$$\begin{bmatrix} v_d \\ v_q \end{bmatrix} = \mathbf{T}_s \begin{bmatrix} V_m \cos\omega_s t \\ V_m \cos\left(\omega_s t - \frac{2\pi}{3}\right) \\ V_m \cos\left(\omega_s t + \frac{2\pi}{3}\right) \end{bmatrix} \tag{3}$$

In order to set the voltage components v_d and v_q, the following corresponding trigonometric identities are applied to the product of two oscillators with different argument:

$$\cos A \cos B = \frac{1}{2}\cos(A+B) + \frac{1}{2}\cos(A-B)$$

$$\sin A \cos B = \frac{1}{2}\sin(A+B) + \frac{1}{2}\sin(A-B)$$

When the oscillator arguments are added, three terms of doubly frequency in both components are presented, which are cancelled due to they are out of phase 120 degrees between them and to have the same modulus; meanwhile when the arguments are subtracted, three identical oscillators are present in both components. Therefore, the utility grid voltage vector in *dq* frame results in:

$$\begin{bmatrix} v_d \\ v_q \end{bmatrix} = \frac{2}{3}\frac{1}{2}\begin{bmatrix} 3V_m \cos(\theta_s - \omega_s t) - 0 \\ -3V_m \sin(\theta_s - \omega_s t) - 0 \end{bmatrix} \tag{4}$$

referring to the *d*- axis with respect to the *a*-phase one (Fig. 2) results that $\theta_s = \omega_s t$, and consequently from (4), $v_d = V_m$ and $v_q = 0$.

Once applied the Park transformation (2) to system (1), the controlled rectifier model in *dq* frame takes the following form:

$$\begin{aligned} \frac{d}{dt}v_{dc} &= \frac{3}{2C_b v_{dc}} v_d i_d - \frac{1}{C_b} i_{dc} \\ \frac{d}{dt}i_d &= -\frac{R_{eq}}{L_{eq}} i_d + \omega_s i_q + \frac{1}{L_{eq}} v_d - \frac{1}{L_{eq}} v_{dr} \\ \frac{d}{dt}i_q &= -\omega_s i_d - \frac{R_{eq}}{L_{eq}} i_q - \frac{1}{L_{eq}} v_{qr} \end{aligned} \tag{5}$$

where v_d, i_d, i_q are the voltage and currents, respectively, in the utility grid, while v_{dr} and v_{qr} are the rectifier input voltages, and ω_s is the grid frequency. Notice that the controlled rectifier model (5) has two inputs v_{dr} and v_{qr}, and consequently two outputs can be controlled. Particularly about this, the output variables are the DC bus voltage and the reactive power.

2.2. The reactive power controller design

For the reactive power controller synthesis is used the block control linearization technique, which begins by defining the DC-voltage error system as:

$$\varepsilon_1 = v_{ref} - v_{dc} \tag{6}$$

whose dynamics is imposed to be:

$$\dot{\varepsilon}_1 = \dot{v}_{ref} - \frac{3}{2C_b v_{dc}} v_d i_d + \frac{1}{C_b} i_{dc} = -K_1 \varepsilon_1 \tag{7}$$

where K_1 is a design parameter used to establish the dynamics rate convergence. The desired dynamics in (7) is achieved through the current control by considering a current reference from solving (7) with respect to i_d, as:

$$i_{ref} = \frac{2C_b v_{dc}}{3v_d}\left(K_1\varepsilon_1 + \dot{v}_{ref} + \frac{1}{C_b} i_{dc}\right) \tag{8}$$

and then, the second error variable is defined for the current as:

$$\varepsilon_2 = i_{ref} - i_d \tag{9}$$

whose dynamics takes the form:

$$\begin{aligned} \dot{\varepsilon}_2 = &-\frac{2C_b}{3v_d}\left(\ddot{v}_{ref} - K_1\dot{v}_{ref} + 2K_1\right)\varepsilon_1 - \left(\frac{R_{eq}}{L_{eq}} + \frac{2\omega_s}{3v_d}\right)\varepsilon_2 \\ &+ \rho_2 + \frac{2C_b}{3L_{eq}v_d} v_{dr} \end{aligned} \tag{10}$$

where:

$$\begin{aligned} \rho_2 = \frac{2C_p}{3v_d}\Bigg[&\ddot{v}_{ref} v_{ref} + \left(\dot{v}_{ref} - \frac{1}{C_b} i_{dc} - 1\right) + K_1 v_{ref} + \frac{2\omega_s}{3v_d} Q_{ref} \\ &+ \frac{R_{eq}}{L_{eq}} i_{ref} - \frac{2}{3v_d} i_{dc} - \frac{1}{L_{eq}} v_d \Bigg] \end{aligned} \tag{11}$$

The third error variable to complete the equivalent system of (5) is defined as the reactive power error variable:

$$\varepsilon_3 = Q_{ref} - Q_s \tag{12}$$

where Q_{ref} is desired reference. And the reactive power dynamics is defined as:

$$\dot{\varepsilon}_3 = \frac{3\omega_s v_d}{2}\varepsilon_2 - \frac{R_{eq}}{L_{eq}}\varepsilon_3 - \rho_3 - \frac{3v_d}{2L_{eq}} v_{qr} \tag{13}$$

where:

$$\rho_3 = -\frac{3\omega_s v_d}{2} i_{ref} + \dot{Q}_{ref} + \frac{R_{eq}}{L_{eq}} Q_{ref} \tag{14}$$

By joining systems (7), (10), and (13), and involving (6), the equivalent model of the controlled rectifier (5) takes the following form:

$$\begin{aligned}\dot{\varepsilon}_1 &= -K_1\varepsilon_1 + \frac{3v_{\mathrm{d}}}{2C_{\mathrm{b}}v_{\mathrm{dc}}}\varepsilon_2\\ \dot{\varepsilon}_2 &= -\frac{4C_{\mathrm{b}}}{3v_{\mathrm{d}}}\varepsilon_1 - \left(\frac{R_{\mathrm{eq}}}{L_{\mathrm{eq}}} + \frac{2\omega_{\mathrm{s}}}{3v_{\mathrm{d}}}\right)\varepsilon_2 + \rho_2 + \frac{2C_{\mathrm{b}}}{3L_{\mathrm{eq}}v_{\mathrm{d}}}v_{\mathrm{dr}}\\ \dot{\varepsilon}_3 &= \frac{3\omega_{\mathrm{s}}v_{\mathrm{d}}}{2}\varepsilon_2 - \frac{R_{\mathrm{eq}}}{L_{\mathrm{eq}}}\varepsilon_3 + \rho_3 - \frac{3v_{\mathrm{d}}}{2L_{eq}}v_{\mathrm{qr}}.\end{aligned} \tag{15}$$

Notice that system (15) has two control inputs, where v_{dr} is used to stabilize in zero the current error ε_2, while v_{qr} is directly employed to force the reactive power error ε_3 to zero. This paper employees the super-twisting controller, where the definition of a sliding surface is required, [12]. In this sense, the sliding surface at d-axis is defined as:

$$s_{\mathrm{d}} = \varepsilon_2 \tag{16}$$

and the corresponding one at q-axis as:

$$s_{\mathrm{q}} = \varepsilon_3 \tag{17}$$

The super-twisting control strategy is robust against external disturbances, parameter uncertainties and their variations, even if required, it is possible to cancel the nonlinear terms of the model, as well as this algorithm exhibits a high-performance response for first-order systems, achieving convergence to zero of the sliding variable in finite time [13–15]. The super-twisting controller is stated as:

$$\begin{aligned}v_i &= \lambda_i|s_i|^{\frac{1}{2}}\operatorname{sign} s_i + u_i\\ \dot{u}_i &= \sigma_i \operatorname{sign} s_i \qquad i = d, q\end{aligned} \tag{18}$$

where λ_i and σ_i are the controller gains. Substituting the super-twisting controller (18) in the rectifier model (15), one obtains:

$$\begin{aligned}\dot{\varepsilon}_1 &= -K_1\varepsilon_1 + \frac{3v_{\mathrm{d}}}{2C_{\mathrm{b}}v_{\mathrm{dc}}}\varepsilon_2\\ \dot{\varepsilon}_2 &= -\frac{4C_{\mathrm{b}}}{3v_{\mathrm{d}}}\varepsilon_1 - \left(\frac{R_{\mathrm{eq}}}{L_{\mathrm{eq}}} + \frac{2\omega_{\mathrm{s}}}{3v_{\mathrm{d}}}\right)\varepsilon_2 + \rho_2 + \frac{2C_{\mathrm{b}}}{3L_{\mathrm{eq}}v_{\mathrm{d}}}\left(\lambda_d|s_d|^{\frac{1}{2}}\operatorname{sign} s_d + u_d\right)\\ \dot{u}_d &= \sigma_d \operatorname{sign} s_d\\ \dot{\varepsilon}_3 &= \frac{3\omega_{\mathrm{s}}v_{\mathrm{d}}}{2}\varepsilon_2 - \frac{R_{\mathrm{eq}}}{L_{\mathrm{eq}}}\varepsilon_3 + \rho_3 - \frac{3v_{\mathrm{d}}}{2L_{eq}}\left(\lambda_d|s_q|^{\frac{1}{2}}\operatorname{sign} s_q + u_q\right)\\ \dot{u}_q &= \sigma_q \operatorname{sign} s_q.\end{aligned} \tag{19}$$

The stability analysis for the closed-loop system (19) is presented in [12,16] by means of proposing a Lyapunov function for each one of the two decoupled subsystems. With respect to the control inputs v_{dr} and v_{qr} in (15), their corresponding gain values for λ_i and σ_i must satisfy the followings restrictions:

$$\begin{aligned}\lambda_{\mathrm{d}} &< \frac{3L_{\mathrm{eq}}v_{\mathrm{d}}}{C_{\mathrm{b}}}\delta_d, \quad \sigma_{\mathrm{d}} > \frac{3L_{eq}v_d}{4C_b}\frac{\lambda_d^2(\delta_d - \lambda_{\mathrm{d}})}{\lambda_d - 2\delta_d}\\ \lambda_{\mathrm{q}} &< \frac{4L_{\mathrm{eq}}}{3v_{\mathrm{d}}}\delta, \quad \sigma_{\mathrm{q}} > \frac{L_{eq}}{3v_d}\frac{\lambda_d^2(\delta_d - \lambda_{\mathrm{d}})}{\lambda_d - 2\delta_d}\end{aligned}$$

where the disturbance norm is assumed to satisfy $|\rho_i| \le \delta_i|s_i|^{\frac{1}{2}}$, with $\delta_i > 0$ [16].

2.3. LCL-filter characterization

An LCL filter is commonly used as a power interface to connect a three-phase converter with the electrical grid, with the aim of reducing the current harmonics caused by the high commutation frequency in the rectifier. Thus, it is required to tune the filter parameters according to the rated active power, the voltage level, and the transistor switching frequency. An LCL filter correctly characterized meets the utility grid interconnection standards.

By considering the utility grid at high frequencies as a short-circuit, the inductance in the rectifier side L_{r} is then estimated by the first-order transfer function as [17]:

$$\frac{i_{\mathrm{i}}(h_{\mathrm{sw}})}{v_{\mathrm{i}}(h_{\mathrm{sw}})} = \frac{1}{\omega_{\mathrm{sw}}L_{\mathrm{r}}} \tag{20}$$

where $i_{\mathrm{i}}(h_{\mathrm{sw}})$ is the inverter current harmonic in its output and $v_{\mathrm{i}}(h_{\mathrm{sw}})$ is the inverter voltage harmonic per phase, both variables at the switching frequency (ω_{sw}). It is recommended a current attenuation between 2 and 3% (20) for defining the converter side inductance value, [17]. Notice that the equivalent inductance of the LCL filter to restrict the voltage drop should be less than 0.1 pu.

By its part, to define the grid side inductance value L_{g}, the following relation is applied [18]:

$$L_{\mathrm{g}} = \frac{\sqrt{\frac{1}{k_{\mathrm{a}}^2}} + 1}{C_f\omega_{\mathrm{sw}}^2} \tag{21}$$

where k_{a} is the relation between injected current toward the grid $i_{\mathrm{g}}(h_{\mathrm{sw}})$ and the inverter generated current $i_{\mathrm{i}}(h_{\mathrm{sw}})$, where no damping resistance is considered for the filter. The preliminary value of the capacitance C_{f} can be determined by taking into account a power factor decrement of 5% at rated power, as recommended in [17], by the following relation:

$$C_{\mathrm{f}} = 0.05C_{\mathrm{b}} \tag{22}$$

with

$$C_{\mathrm{b}} = \frac{1}{\omega_{\mathrm{g}}Z_{\mathrm{b}}} \tag{23}$$

$$Z_{\mathrm{b}} = \frac{V_{\mathrm{LL}}^2}{P_{\mathrm{b}}} \tag{24}$$

where ω_{g} is the utility grid frequency, P_{b} is the rated active power, while V_{LL} is the line-to-line voltage. Both, Z_{b} and C_{b} are the base values of the impedance and capacitance, respectively [17]. In addition, the preliminary value of C_{f}(22) can be adjusted to position the resonant frequency f_{res} near the left side of the midpoint of the frequency range, which is defined from ten times the utility-grid frequency ($10f_{\mathrm{g}}$) to the converter switching frequency (f_{sw}) [17].

Nevertheless, the approximated value of C_{f}(22) can be modified to locate the resonance frequency f_{res} near of the left side of the middle point of the frequency range, described above. The resonant frequency ω_{res} is calculated by [18]

$$\omega_{\mathrm{res}} = \sqrt{\frac{L_{\mathrm{r}} + L_{\mathrm{g}}}{L_{\mathrm{r}}L_{\mathrm{g}}C_{\mathrm{f}}}} \tag{25}$$

and it is possible to make parametric analysis using the Bode diagram to locate different resonant points at different capacitance values using the following transfer function:

$$\frac{I_{\mathrm{g}}(s)}{V_{\mathrm{r}}(s)} = \frac{1}{C_{\mathrm{f}}L_{\mathrm{r}}L_{\mathrm{g}}s^3 + (L_{\mathrm{r}} + L_{\mathrm{g}})s} \tag{26}$$

and then, from the Bode diagram, the previous capacitance value is updated considering the best location of the resonant points.

Finally, a resistor in series with the capacitor is used to damp the resonant frequency. The value of resistance R_{f} is defined as

the capacitor impedance value divided by three at the resonant frequency ω_{res}, and can be calculated by [19]

$$R_f = \frac{1}{3\,\omega_{res} C_f} \tag{27}$$

However, the value of R_f can be modified through a parametric analysis using the Bode diagram applying the following transfer function:

$$\frac{I_g(s)}{V_r(s)} = \frac{R_f C_f s + 1}{L_r L_g C_f s^3 + (L_r + L_g) R_f C_f s^2 + (L_r + L_g) s} \tag{28}$$

and thus, from the Bode plot, the resistance value R_f is selected such that produces the best frequency response.

3. Induction motor model

The induction motor type squirrel-cage is widely used in the drive units of industrial machinery; the motor construction is rough and robust, free of maintenance, and it has a good speed regulation. However its model is very complex and represents a control challenge in a closed-loop system. The voltage and magnetic flux linkages vector equations for the stator winding are [20]:

$$\begin{aligned} \mathbf{v}_{ABC} &= \mathbf{R}_s \mathbf{i}_{ABC} + \frac{d}{dt}\boldsymbol{\lambda}_{ABC} \\ \boldsymbol{\lambda}_{ABC} &= \mathbf{L}_s \mathbf{i}_{ABC} + \mathbf{L}_{sr} \mathbf{i}_{abc} \end{aligned} \tag{29}$$

where $\mathbf{v}_{ABC}$, $\mathbf{i}_{ABC}$, and $\boldsymbol{\lambda}_{ABC}$ are, respectively, the stator winding voltage, current, and magnetic flux vectors; meanwhile, $\mathbf{i}_{abc}$ is the induced rotor current vector with respect to the stator-side; $\mathbf{R}_s$ is a diagonal matrix where each component is the stator resistance per phase; $\mathbf{L}_s$ and $\mathbf{L}_{sr}$ are the self and mutual inductance matrices respectively, which are defined as:

$$\mathbf{L}_s = \begin{bmatrix} L_{ss} & L_{sm} & L_{sm} \\ L_{sm} & L_{ss} & L_{sm} \\ L_{sm} & L_{sm} & L_{ss} \end{bmatrix}$$

$$\mathbf{L}_{sr} = L_{srm} \begin{bmatrix} \cos\theta_r & \cos\left(\theta_r + \frac{2\pi}{3}\right) & \cos\left(\theta_r - \frac{2\pi}{3}\right) \\ \cos\left(\theta_r - \frac{2\pi}{3}\right) & \cos\theta_r & \cos\left(\theta_r + \frac{2\pi}{3}\right) \\ \left(\theta_r + \frac{2\pi}{3}\right) & \left(\theta_r - \frac{2\pi}{3}\right) & \cos\theta_r \end{bmatrix}$$

where θ_r is the phase-*a* rotor magnetic axis position related to the phase-*A* stator magnetic axis; L_{ss} is the stator self-inductance per phase, L_{srm} is the maximum value of the stator and rotor mutual-inductance, and finally L_{sm} is the two phases of the stator mutual-inductance. On the other hand, the voltage and magnetic flux linkages vector equations for the induced three-phase rotor winding are:

$$\begin{aligned} \mathbf{0} &= \mathbf{R}_r \mathbf{i}_{abc} + \frac{d}{dt}\boldsymbol{\lambda}_{abc} \\ \boldsymbol{\lambda}_{abc} &= \mathbf{L}_{sr}^{\top} \mathbf{i}_{ABC} + \mathbf{L}_r \mathbf{i}_{abc} \end{aligned} \tag{30}$$

where the induced rotor voltage vector $\mathbf{v}_r$ is equated to zero, due to the conductors of the rotor winding being short-circuited at the ends; $\boldsymbol{\lambda}_{abc}$ is the rotor winding magnetic flux linkages vector, referred to the generator-side; $\mathbf{R}_r$ is a diagonal matrix, where each component is the rotor resistance per phase with respect to the stator-side; and $\mathbf{L}_r$ is the rotor self-inductance matrix stated as:

$$\mathbf{L}_r = \begin{bmatrix} L_{rr} & L_{rm} & L_{rm} \\ L_{rm} & L_{rr} & L_{rm} \\ L_{rm} & L_{rm} & L_{rr} \end{bmatrix}$$

where L_{rm} is the two phases rotor mutual-inductance, while L_{rr} is the per phase rotor self-inductance, both inductances are referred to the stator-side.

Any induction motor model derived from systems (29) and (30) will have variant coefficients with the time due to rotor and stator mutual inductances vary with respect to the rotor position. Hence, a common practice is to refer the stator voltage and magnetic flux linkages system (29) to the stationary $\alpha\beta$ coordinate system, applying the similitude transformation (2) with $\theta_s = 0$, taking the following form [20]:

$$\mathbf{T}_{\alpha\beta 0} = \frac{2}{3}\begin{bmatrix} 1 & -\frac{1}{2} & -\frac{1}{2} \\ 0 & \frac{\sqrt{3}}{2} & -\frac{\sqrt{3}}{2} \\ \frac{\sqrt{2}}{2} & \frac{\sqrt{2}}{2} & \frac{\sqrt{2}}{2} \end{bmatrix} \tag{31}$$

Hence, the voltage and magnetic flux linkages vector equations of the stator winding in $\alpha\beta$ coordinate system become

$$\begin{aligned} \begin{bmatrix} v_{\alpha s} \\ v_{\beta s} \end{bmatrix} &= \begin{bmatrix} r_s & 0 \\ 0 & r_s \end{bmatrix}\begin{bmatrix} i_{\alpha s} \\ i_{\beta s} \end{bmatrix} + \frac{d}{dt}\begin{bmatrix} \lambda_{\alpha s} \\ \lambda_{\beta s} \end{bmatrix} \\ \begin{bmatrix} \lambda_{\alpha s} \\ \lambda_{\beta s} \end{bmatrix} &= \begin{bmatrix} L_s & 0 \\ 0 & L_s \end{bmatrix}\begin{bmatrix} i_{\alpha s} \\ i_{\beta s} \end{bmatrix} + \begin{bmatrix} L_m & 0 \\ 0 & L_m \end{bmatrix}\begin{bmatrix} i_{\alpha r} \\ i_{\beta r} \end{bmatrix} \end{aligned} \tag{32}$$

where

$$L_s = L_{ss} - L_{sm} \tag{33}$$

and

$$L_m = \frac{3}{2} L_{srm}. \tag{34}$$

On the other hand, the rotor voltage and magnetic flux linkages system (30) are referred to the stationary $\alpha\beta$ coordinate system, applying the similitude transformation (31), to obtain

$$\begin{aligned} \begin{bmatrix} v_{\alpha r} \\ v_{\beta r} \end{bmatrix} &= \begin{bmatrix} r_r & 0 \\ 0 & r_r \end{bmatrix}\begin{bmatrix} i_{\alpha r} \\ i_{\beta r} \end{bmatrix} + \frac{d}{dt}\begin{bmatrix} \lambda_{\alpha r} \\ \lambda_{\beta r} \end{bmatrix} \\ \begin{bmatrix} \lambda_{\alpha r} \\ \lambda_{\beta r} \end{bmatrix} &= \begin{bmatrix} L_m & 0 \\ 0 & L_m \end{bmatrix}\begin{bmatrix} i_{\alpha s} \\ i_{\beta s} \end{bmatrix} + \begin{bmatrix} L_r & 0 \\ 0 & L_r \end{bmatrix}\begin{bmatrix} i_{\alpha r} \\ i_{\beta r} \end{bmatrix} \end{aligned} \tag{35}$$

where

$$L_r = L_{rr} - L_{rm}. \tag{36}$$

Systems (32) and (35) are reduced order with respect to systems (29) and (30) in *abc* frame, because of the zero sequence components of the electrical variables are not present. The induction motor is an electromechanical device whose mechanical part is described by:

$$J_m \frac{d}{dt}\omega_m = T_e - B_m \omega_m - T_L \tag{37}$$

where ω_m is the rotor speed; T_e and T_L represent the motor electromagnetic torque and the load torque, respectively;

J_m and B_m are the inertia moment and frictional coefficient of the rotor, respectively. The torque T_e is derived from the magnetic stored energy, which is defined as [20]:

$$W_f = \frac{1}{2}\left(\mathbf{i}_{ABC}\right)^{\top}\mathbf{L}_{ss}\mathbf{i}_{ABC} + \left(\mathbf{i}_{ABC}\right)^{\top}\mathbf{L}_{sr}\mathbf{i}_{abc} + \frac{1}{2}\left(\mathbf{i}_{abc}\right)^{\top}\mathbf{L}_{rr}\mathbf{i}_{abc} \tag{38}$$

and by computing the definition of the electromagnetic torque, one obtains:

$$T_e = \frac{\partial}{\partial\theta_r} W_f = \left(\frac{P}{2}\right)\frac{d}{d\theta_r}\left[\left(\mathbf{i}_{ABC}\right)^{\top}\mathbf{L}_{sr}\mathbf{i}_{abc}\right] \tag{39}$$

Applying the transformations (2) and (31) with $\theta_s = \theta_r$ to stator and rotor current vector in (39), respectively, and involving (34), the torque T_L in the $\alpha\beta$ coordinate system takes the form:

$$T_e = \frac{3P}{4} L_m \mathbf{i}_{\alpha\beta s}^{\top}\begin{bmatrix} 0 & 1 \\ -1 & 0 \end{bmatrix}\mathbf{i}_{\alpha\beta r} \tag{40}$$

By solving (32) for rotor current vector, and substituting in (40), it yields:

$$T_e = \frac{3P}{4}\frac{L_m}{L_r}\left(i_{\beta s}\lambda_{\alpha r} - i_{\alpha s}\lambda_{\beta r}\right) \tag{41}$$

Using (41) in (37), and solving (32) for the stator currents, and (35) for the rotor flux linkages, the model for the squirrel-cage induction motor at the stationary $\alpha\beta$ coordinate frame is obtained as follows [21]:

$$\begin{aligned}\frac{d\omega_m}{dt} &= K_r\boldsymbol{\lambda}_r^\top \mathbf{M}\mathbf{i}_s - \frac{B_m}{J_m}\omega_m - \frac{1}{J_m}T_L\\ \frac{d\boldsymbol{\lambda}_r}{dt} &= \mathbf{A}_{11}\boldsymbol{\lambda}_r - \gamma\mathbf{i}_s\\ \frac{d\mathbf{i}_s}{dt} &= \mathbf{A}_{21}\boldsymbol{\lambda}_r + \frac{L_m}{T_r}\mathbf{i}_s + \frac{1}{\sigma L_s}\mathbf{v}_s\end{aligned} \tag{42}$$

where the flux linkages of rotor winding, current and voltage of stator winding vectors in $\alpha\beta$ coordinate system are:

$$\boldsymbol{\lambda}_\mathrm{r} = [\ \lambda_{\alpha\mathrm{r}}\quad \lambda_{\beta\mathrm{r}}\ ]^\top,\ \mathbf{i}_\mathrm{s} = [\ i_{\alpha\mathrm{s}}\quad i_{\beta\mathrm{s}}\ ]^\top,\ \mathbf{v}_\mathrm{s} = [\ v_{\alpha\mathrm{s}}\quad v_{\beta\mathrm{s}}\ ]^\top$$

where the load torque T_L becomes a mechanical external input, which is considered as a disturbance for the induction motor model. The corresponding matrices are defined as

$$\mathbf{M} = \begin{bmatrix} 0 & 1\\ -1 & 0\end{bmatrix}$$

and

$$\mathbf{A}_{11} = \begin{bmatrix} -\frac{1}{T_\mathrm{r}} & -\frac{P}{2}\omega_\mathrm{m}\\ \frac{P}{2}\omega_\mathrm{m} & -\frac{1}{T_\mathrm{r}}\end{bmatrix},\quad \mathbf{A}_{21} = \begin{bmatrix} \frac{\delta}{T_\mathrm{r}} & \frac{P}{2}\delta\omega_\mathrm{m}\\ -\frac{P}{2}\delta\omega_\mathrm{m} & \frac{\delta}{T_\mathrm{r}}\end{bmatrix}$$

where

$$K_\mathrm{T} = \frac{3PL_\mathrm{m}}{4J_\mathrm{m}L_\mathrm{r}},\quad \sigma = 1 - \frac{L_\mathrm{m}^2}{L_\mathrm{s}L_\mathrm{r}}$$

$$\delta = \frac{1-\sigma}{\sigma L_\mathrm{m}},\quad \gamma = \frac{1}{\sigma T_\mathrm{s}} + \frac{1-\sigma}{\sigma T_\mathrm{r}}$$

with

$$T_\mathrm{r} = \frac{L_\mathrm{r}}{R_\mathrm{r}},\ T_s = \frac{L_s}{R_s},\ L_\mathrm{m} = \frac{3}{2}L_\mathrm{mag}$$

$$L_\mathrm{s} = L_\mathrm{ls} + L_\mathrm{m}$$

and

$$L_\mathrm{r} = L_\mathrm{lr} + L_\mathrm{m}$$

being L_mag the magnetizing inductance; L_ls is the stator leakage inductance, and L_lr becomes the rotor leakage inductances. The model inductances L_r, L_s and L_m in (42) are defined from the equivalent circuit inductances L_mag, L_ls, and L_lr, through equations given in [21].

4. Speed controller for the induction motor

The induction motor speed controller synthesis begins applying the state-feedback linearization strategy to the motor model for obtaining an equivalent model in the controllable canonical form. In the controller design is necessary to decouple the corresponding inputs, to estimate the derivative with respect to time of tracking error, and to estimate the rotor flux linkages through a rotor fluxes robust observer.

4.1. State feedback linearization technique

Non-linear systems could be controlled by applying the feedback linearization methodology. for this purpose, a transformation is applied to the system model to be controlled in order to obtain the controllable canonical form through the definition of error variables. Therefore, the original tracking problem is resolved by stabilizing the tracking error variables and driving them to the origin. In this transformation, the control input cancels the nonlinear terms and improves the eigenvalue placement to obtain a faster vanishing of the error variables of the new linear system.

The induction motor model (42) on the $\alpha\beta$ framework represents a two-phase induction machine with constants coefficients, which results equivalent to the three-phase model in *abc* coordinates. This model is highly non-linear and has two control inputs that supplies voltage to $\alpha\beta$ equivalent stator winding, $v_{\alpha s}$ and $v_{\beta s}$; therefore, two output variables can be controlled, particularly the selected variables are the speed of the motor ω_m and the rotor flux squared modulus ϕ_r. The controller design is based on the induction motor model, where the tracking error is established as:

$$\boldsymbol{\varepsilon}_1 = \begin{bmatrix}\varepsilon_\omega\\ \varepsilon_\phi\end{bmatrix} = \begin{bmatrix}\omega_\mathrm{ref} - \omega_\mathrm{m}\\ \phi_\mathrm{ref} - \phi_\mathrm{r}\end{bmatrix} \tag{43}$$

where ω_ref and ϕ_ref are the references to be tracked by the output variables, and ϕ_r is calculated as

$$\phi_\mathrm{r} = |\ \boldsymbol{\lambda}_\mathrm{r}\ |^2 = \boldsymbol{\lambda}_\mathrm{r}^\top\boldsymbol{\lambda}_\mathrm{r} = \lambda_{\alpha\mathrm{r}}^2 + \lambda_{\beta\mathrm{r}}^2 \tag{44}$$

Involving the induction motor model (42), and matching the dynamics of the tracking error vector (43) with a new error vector variable $\boldsymbol{\varepsilon}_2$, results in:

$$\dot{\boldsymbol{\varepsilon}}_1 = \begin{bmatrix}\dot{\omega}_\mathrm{ref} + \frac{1}{T_\mathrm{m}}\omega_\mathrm{m}\\ \dot{\phi}_\mathrm{ref} + \frac{2}{T_\mathrm{r}}\phi_\mathrm{r}\end{bmatrix} - \begin{bmatrix}K_\mathrm{T}\boldsymbol{\lambda}_\mathrm{r}^\top\mathbf{M}\\ 2\frac{L_\mathrm{m}}{T_\mathrm{r}}\boldsymbol{\lambda}_\mathrm{r}^\top\end{bmatrix}\mathbf{i}_\mathrm{s} + \begin{bmatrix}\frac{1}{J_\mathrm{m}}T_\mathrm{L}\\ 0\end{bmatrix} = \boldsymbol{\varepsilon}_2 \tag{45}$$

and calculating the dynamics of $\boldsymbol{\varepsilon}_2$, yields:

$$\dot{\boldsymbol{\varepsilon}}_2 = \mathbf{F}_2 - \mathbf{B}_2\left(\lambda_\mathrm{r}\right)\mathbf{v}_\mathrm{s} \tag{46}$$

where:

$$\begin{aligned}\mathbf{F}_2 = &\begin{bmatrix}\ddot{\omega}_\mathrm{ref} + \frac{1}{T_\mathrm{m}}\dot{\omega}_\mathrm{ref} + \frac{1}{J_\mathrm{m}}\dot{T}_\mathrm{L}\\ \dot{\phi}_\mathrm{ref}\end{bmatrix} + \phi_\mathrm{r}\begin{bmatrix}-\frac{P}{2}K_\mathrm{T}\delta\omega_\mathrm{m}\\ \frac{4L_\mathrm{m}\delta}{T_\mathrm{r}^2} + \frac{2}{T_\mathrm{r}}\end{bmatrix}\\ &- \begin{bmatrix}-\frac{K_\mathrm{T}}{T_\mathrm{r}}(1-\delta T_\mathrm{r})\boldsymbol{\lambda}_r\mathbf{M} + \frac{P}{2}K_\mathrm{T}\omega_m\boldsymbol{\lambda}_\mathrm{r}^\top\\ 2\frac{L_\mathrm{m}}{T_\mathrm{r}}(1+\gamma+\frac{P}{2}\omega_\mathrm{m} - \frac{1}{T_\mathrm{r}})\boldsymbol{\lambda}_\mathrm{r}^\top + \frac{2L_\mathrm{m}^2}{T_\mathrm{r}^2}\mathbf{i}_\mathrm{s}^\top\end{bmatrix}\mathbf{i}_\mathrm{s}\end{aligned} \tag{47}$$

and

$$\begin{aligned}\mathbf{B}_2(\boldsymbol{\lambda}_\mathrm{r}) &= \frac{1}{\sigma L_\mathrm{s}}\begin{bmatrix}K_\mathrm{T}\boldsymbol{\lambda}_\mathrm{r}^\top\mathbf{M}\\ 2\frac{L_\mathrm{m}}{T_\mathrm{r}}\boldsymbol{\lambda}_\mathrm{r}^\top\end{bmatrix}\\ &= \frac{1}{\sigma T_\mathrm{r}L_\mathrm{s}}\begin{bmatrix}-K_\mathrm{T}T_\mathrm{r}\lambda_{\beta\mathrm{r}} & K_\mathrm{T}T_\mathrm{r}\lambda_{\alpha\mathrm{r}}\\ 2L_\mathrm{m}\lambda_{\alpha\mathrm{r}} & 2L_\mathrm{m}\lambda_{\beta\mathrm{r}}\end{bmatrix}\end{aligned} \tag{48}$$

Joining (45) and (46) an equivalent system of (42) is obtained as follows:

$$\begin{aligned}\dot{\boldsymbol{\varepsilon}}_1 &= \boldsymbol{\varepsilon}_2\\ \dot{\boldsymbol{\varepsilon}}_2 &= \mathbf{F}_2 - \mathbf{B}_2(\boldsymbol{\lambda}_\mathrm{r})\mathbf{v}_\mathrm{s}\end{aligned} \tag{49}$$

With the purpose of setting a robust controller (49), a new system takes the form:

$$\mathbf{s} = \mathbf{C}_1\boldsymbol{\varepsilon}_1 + \boldsymbol{\varepsilon}_2 \tag{50}$$

whose dynamics is:

$$\dot{\mathbf{s}} = \mathbf{C}_1\boldsymbol{\varepsilon}_2 + \mathbf{F}_2 - \mathbf{B}_2(\boldsymbol{\lambda}_\mathrm{r})\mathbf{v}_\mathrm{s} \tag{51}$$

System (51) has relative degree equal to 1, but a coupling exists between the control input and the rotor flux linkages, as pointed in (49). Therefore, an additional transformation can be proposed to obtain an uncoupling system:

$$\mathbf{s}^* = \mathbf{B}_2^{-1}(\boldsymbol{\lambda}_\mathrm{r})\mathbf{s} \tag{52}$$

with dynamics:

$$\dot{\mathbf{s}}^* = \mathbf{F}_2^* - \mathbf{v}_\mathrm{s} \tag{53}$$

where:

$$\mathbf{F}_2^* = \dot{\mathbf{B}}_2^{-1}(\boldsymbol{\lambda}_\mathrm{r})\mathbf{B}_2(\boldsymbol{\lambda}_\mathrm{r})\mathbf{s}^* + \mathbf{B}_2^{-1}(\boldsymbol{\lambda}_\mathrm{r})\mathbf{C}_1\boldsymbol{\varepsilon}_2 + \mathbf{B}_2^{-1}(\boldsymbol{\lambda}_\mathrm{r})\mathbf{F}_2$$

therefore, system (53) is decoupled and becomes of reduced order. Consequently, applying the super-twisting control law in (53) yields:

$$\begin{aligned}\dot{\mathbf{s}}^* &= \mathbf{F}_2^* - \boldsymbol{\lambda}|\mathbf{s}^*|^{\frac{1}{2}}\,\text{sign}(\mathbf{s}^*) + \mathbf{u}\\ \dot{\mathbf{u}} &= -\boldsymbol{\sigma}\,\text{sign}(\mathbf{s}^*)\end{aligned} \tag{54}$$

being $\boldsymbol{\lambda}$ and $\boldsymbol{\sigma}$ the corresponding controller gains selected with high enough values to guarantee that the sliding variables $\mathbf{s}^*$(52) and its first-order time derivative $\dot{\mathbf{s}}^*$(53) move toward zero, and consequently the sliding surface $\mathbf{s}$(50) is forced to the origin in finite time. Consequently, an asymptotic motion to zero is achieved for both the speed tracking error and rotor flux modulus regulation error. Thus, the control goal is fulfilled, where the controlled outputs achieve their reference values. In [12] is presented the stability analysis for the system (54), where the values range for the super-twisting controller gains λ and σ are defined. The analysis is based on the Lyapunov theory as described in [16], then the asymptotic stability of the system is demonstrated; as a consequence, the constraints for controller gains can be obtained from:

$$\begin{aligned}&\lambda_i > 2\delta_i\\ &\sigma_i > \frac{1}{2}\frac{\lambda_i^2(\delta_i - \lambda_i)}{\lambda_i - 2\delta_i}\end{aligned} \tag{55}$$

by considering that the disturbance term fulfill the bound $|F_2^*| \leq \delta_i|s_i|^{\frac{1}{2}}$, for a positive constant value of δ_i [16]. Note that the precise knowledge of F_2^* in (54) is no necessarily required for the controller design to guarantee the stability, but to ensure the disturbance is accordingly bounded. In this sense, by considering physical restrictions for the system, as well as a bounded operation range of the variables, it will result in a bounded value for $\mathbf{F}_2^*$.

4.2. Robust differentiator

For a given measurable function $f(t)$, it is possible to determine its time derivative via a first-order differentiator, by considering that is composed of an unknown base function $f_0(t)$ containing noise. The $f(t)$ is defined into $[0, \infty)$, with a Lipschitz constant $L > 0$ [22,23]. The differentiator is used to obtain in real-time an estimation of $f_0(t)$ and its time derivative, i.e., $\dot{f}_0(t)$. The procedure for the robust differentiator design is as follows. Then, let us define the system

$$\dot{z} = v(x) \tag{56}$$

where $v(x)$ is an input function which depends on the difference $x = z - f_0(t)$, and whose objective is to ensure that $x = 0$, and consequently $\dot{x} = 0$, hence, one obtains $z = f_0(t)$ and $\dot{f}_0(t) = v$. Thus, (56) can be described as

$$\dot{x} = -\dot{f}_0(t) + v,\ \ |\ddot{f}_0| \leq L \tag{57}$$

Then, by applying the super-twisting algorithm as input $v(x)$ into (57), the differentiator takes the form:

$$\begin{aligned}\dot{z} = v(x) &= -\lambda_1\,|\,z - f_0(t)\,|^{\frac{1}{2}}\,\text{sign}(z - f_0(t)) + z_1\\ \dot{z}_1 &= -\lambda_2\text{sign}(z - f_0(t))\end{aligned} \tag{58}$$

where v or z_1 can be taken as the differentiator output [22,23]. Evaluating the following constraints to tune the differentiator

$$L < \lambda_2 \qquad \text{and} \qquad \frac{2(\lambda_2 + L)^2}{\lambda_1^2(\lambda_2 - L)} < 1 \tag{59}$$

both v and z_1 converge to $\dot{f}_0(t)$ in a finite time, while z converges to $f_0(t)$, which is reached by appropriately selecting the values for λ_1 and λ_2.

4.3. Observer synthesis of the rotor flux linkages

For the implementation of the motor controller (54), the full state variables must be available for regulating the speed and the rotor flux linkages squared modulus. For this purpose, the rotor speed ω_m and stator current vector $\mathbf{i}_s$ are measured variables; nonetheless, the rotor flux linkages variables are not available, therefore, they are estimated via a sliding-mode observer, as described in [24]. The rotor flux observer synthesis is based on the induction motor model (42), where the rotor speed is considered a known variable and therefore, the mechanical state equation is omitted. Hence, the proposed observer results in:

$$\begin{aligned}\frac{d\hat{\boldsymbol{\lambda}}_r}{dt} &= \mathbf{A_{11}}\hat{\boldsymbol{\lambda}}_r - \gamma\hat{\mathbf{i}}_s - \mathbf{G}_1\mathbf{v}\\ \frac{d\hat{\mathbf{i}}_s}{dt} &= \mathbf{A_{21}}\hat{\boldsymbol{\lambda}}_r + \frac{L_m}{T_r}\hat{\mathbf{i}}_s + \frac{1}{\sigma L_s}\mathbf{v_s} + \mathbf{v}\end{aligned} \tag{60}$$

with

$$\mathbf{G}_1 = \begin{bmatrix} g_{11} & 0\\ 0 & g_{22}\end{bmatrix}$$

and

$$\mathbf{v} = \mathbf{M}\,\text{sign}\left(\mathbf{i}_s - \hat{\mathbf{i}}_s\right), \qquad \mathbf{M} = \begin{bmatrix} m_{11} & 0\\ 0 & m_{22}\end{bmatrix}$$

where the scalar entries in $\mathbf{G}_1$ and $\mathbf{M}$ are positive observer gains, meanwhile, $\mathbf{v}$ is a discontinuous input to ensure convergence.

For the observer performance analysis, the estimation error variables are defined as $\tilde{\boldsymbol{\lambda}}_r = \boldsymbol{\lambda}_r - \hat{\boldsymbol{\lambda}}_r$ and $\tilde{\boldsymbol{i}}_s = \boldsymbol{i}_s - \hat{\boldsymbol{i}}_r$, then from system (42) and the robust observer (60), the dynamics of the estimation error becomes:

$$\begin{aligned}\frac{d\tilde{\boldsymbol{\lambda}}_r}{dt} &= \mathbf{A}_{11}\tilde{\boldsymbol{\lambda}}_r - \gamma\tilde{\mathbf{i}}_s + \mathbf{G}_1\mathbf{v}\\ \frac{d\tilde{\mathbf{i}}_s}{dt} &= \mathbf{A}_{21}\tilde{\boldsymbol{\lambda}}_r + \frac{L_m}{T_r}\tilde{\mathbf{i}}_s - \mathbf{v}\end{aligned} \tag{61}$$

where the discontinuous input $\mathbf{v}$ acts as an equivalent control v_{eq} to steer the sliding surface $\tilde{\mathbf{i}}_s$ toward zero. Considering that $\tilde{\mathbf{i}}_s = 0$, the equivalent control of the observer can be obtained from the steady-state current equation in (61), which becomes:

$$\mathbf{v}_{eq} = \mathbf{A}_{21}\tilde{\boldsymbol{\lambda}}_r \tag{62}$$

Applying the equivalent control (62) at the rotor flux equation in (61), one obtains the resulting flux error dynamics as:

$$\frac{d}{dt}\tilde{\boldsymbol{\lambda}}_r = (\mathbf{A}_{11} + \mathbf{G}_1\mathbf{A}_{21})\,\tilde{\boldsymbol{\lambda}}_r$$

where the entries of $\mathbf{G}_1$ are selected to establish the rate convergence of $\tilde{\boldsymbol{\lambda}}_r$. The observer performance with discontinuous input shows robustness in presence of disturbances and measurements noise [25].

5. Experimental results

The two cascade controllers are validated through a test prototype for regulating the reactive power fed to the electrical network and controlling the induction motor speed. The first controller comprises the reactive power control system, integrated by the electrical network that feeds a three-phase LCL filter connected with the SEMIKRON converter, and finally the DC bus with a capacitor, such as shown in Fig. 3. The line-to-line currents and voltages of the electrical grid are sensed, meanwhile, the control input signals of the reactive power controller are digitally handled by the space vector pulse width modulation (SVPWM). The second controller corresponds to the

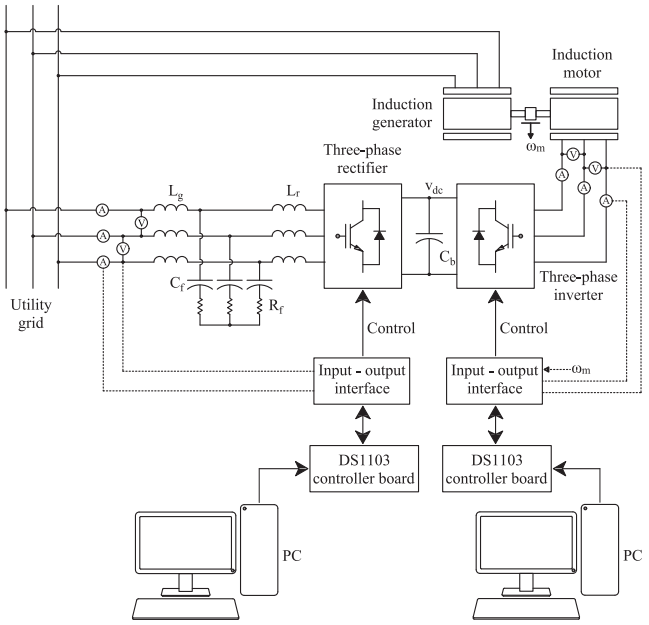

Fig. 3. Cascade control system scheme.

Table 1
Motor model ratings and parameters referred to the stator winding.

Parameter	Value
Power	3/4 HP
Rated Voltage	208-230/460 V
Rated current	2.3-3/1.5 A
Rated speed	1725 r.p.m.
Stator resistance, R_s	2.5 Ω
Rotor resistance, R_r	2.5 Ω
Inductance stator, L_s	0.2260 H
Magnetizing inductance, L_m	0.2165 H
Inductance rotor, L_r	0.2260 H
Inertial moment, J_m	0.0055 N m s^2
Frictional coefficient, B_m	0.0018 N m s

motor induction speed control system which is composed of a squirrel-cage induction motor (3/4 HP Baldor) that impulses an induction generator (1/4 HP LabVolt), which is used to vary the motor load, a SEMIKRON three-phase bridge inverter which feds the induction motor (Fig. 3). The line currents and line-to-line voltages are sensed in motor terminals, meanwhile the motor speed is sensed through a BEI encoder, whose resolution is 2048 pulses; finally, the control input signals of the speed controller are conditioned by the SVPWM technique. Fig. 4 depicts the complete workbench implemented in the laboratory. The motor model parameters are described in Table 1. For the controller implementation, the dSPACE DS1103 data acquisition/processing board is employed, to process the input/output variables, tune the controller gains, and display the system variables. The board is handled by Matlab/Simulink, which allows implementing high-level programming, where the required code is efficiently and directly generated by the Simulink compiler. The board is configured to operate using the Euler solver, with a sample time of 150 μs for the reactive power control, while 100 μs for the induction motor speed regulation; these time scales ensure to properly management the controlled system dynamics and the corresponding activation frequency of the IGBTs at 3300 Hz and 4680 Hz, respectively.

Fig. 4. Laboratory experimental setup.

5.1. Experiment design

To show the cascade control system robustness, advantages, and performance, the experimental results are exposed. The cascade control scheme is constituted by: (a) the reactive power controller, where sudden changes in the active power are applied as external disturbances; and (b) the induction motor speed controller, where abrupt variations in the load torque represent the corresponding external disturbances. An experimental test was configured using a 220 V line-to-line utility grid voltage, and the reactive power is regulated at 300 VAr's, meanwhile, the DC link bus located between the two converters is regulated at 270 V. Notice that the power factor is improved through the reactive power that is delivered to the electrical grid. On the other hand, the induction motor speed tracks a reference signal, which presents sudden variations upper synchronous speed from 1820 to 1900 *r.p.m.*, as done in [26]; these changes cause variations in load torque and active power, due to an induction generator connected to the utility grid is used as load. Meanwhile, the rotor flux linkages squared modulus is regulated at 0.02 wb^2.

5.2. Results of the reactive power control

Fig. 5 shows the reactive power tracking performance where is regulated the reactive power effectively at −300 VAr's in presence of external disturbances produced by the active power variations when changes in the motor load are presented, as is depicted in Fig. 5 (a). The steady-state reactive power is −298 VAr's, then the steady-state error is 0.67%. It is presented a sudden change falling edge in the active power of the induction motor at 3.4 s when the motor speed downs from 1900 to 1810 r.p.m., the reactive power presents an oscillation having a settling time and an overshoot of 0.36 s and 183%, respectively. Meanwhile, the DC voltage is regulated correctly at 270 V, as pictured in Fig. 5 (b), where a steady-state error of 0.37% is exhibited. The DC bus voltage presents an oscillation at 3.4 s with a settling time of 0.32 s and an undershot of 2% when the motor speed downs suddenly. The control inputs performance is pictured in Fig. 6. The motion of the DC bus voltage error ε_1 is asymptotic (see Fig. 6 (a) when the current error at d-axis ε_2 goes to zero in finite time (Fig. 6 (b) because of the action of the control input v_d (Fig. 6 (c), where the sliding surface ε_2 has an oscillation with a settling time of 0.32 s. Meanwhile, the current error motion at q-axis ε_3 goes to zero in finite time (Fig. 6 (b) as a result of the input control v_{qr} (Fig. 6 (c), where the ε_3 presents an oscillation with a settling

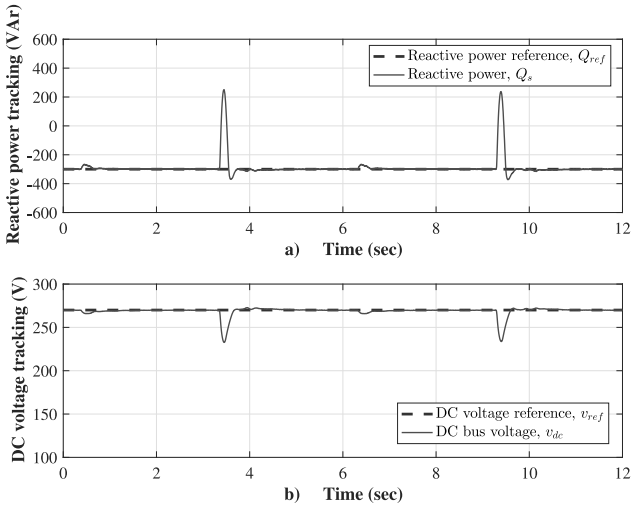

Fig. 5. Reactive power control system performance: (a) Reactive power, and (b) DC bus voltage.

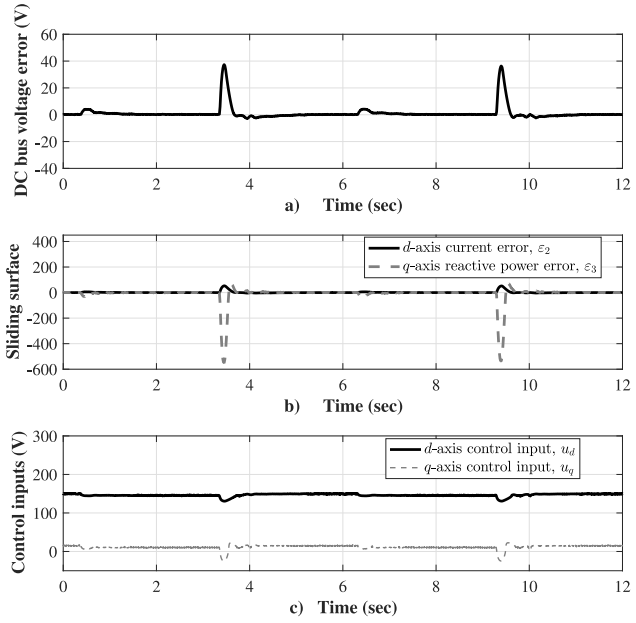

Fig. 6. The control input performance: (a) DC bus voltage error, (b) Sliding surface, and (c) Control inputs.

time of 0.36 s. The control input v_{dr} varies from 146 to 150 V and v_{qr} changes from 12 to 16 V, when the active power falls in the induction motor, (Fig. 6 (c). In Fig. 7 (a), the reactive power is regulated in −300 VAr's, which are delivered to the utility grid. In Fig. 7 (b) the phase-B current i_b leads 64.8° to the phase-voltage v_{bn}, which confirms that the power factor is leading.

It is worth mentioning that parameter uncertainties in the physical systems may exist, which are taken into account in the disturbance terms. By its part, the controller design considers that those disturbances are bounded to ensure convergence. Indeed, an essential feature of sliding-mode-based controllers is their ability to be robust against unknown uncertainties/disturbances. The controller robustness is demonstrated in the experimental results, where the control objectives are being carried out although the parameter values could have uncertainties.

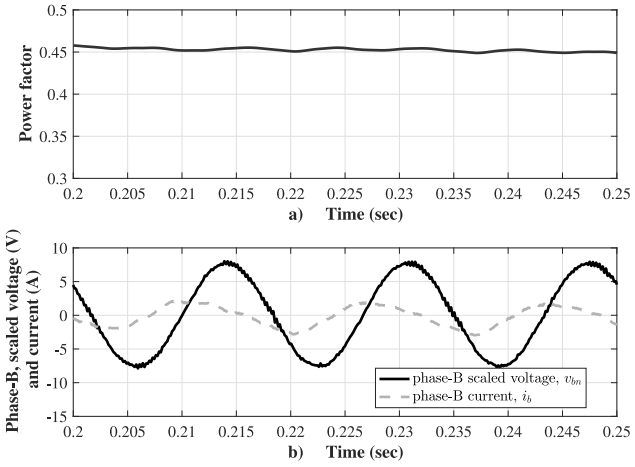

Fig. 7. Leading power factor.

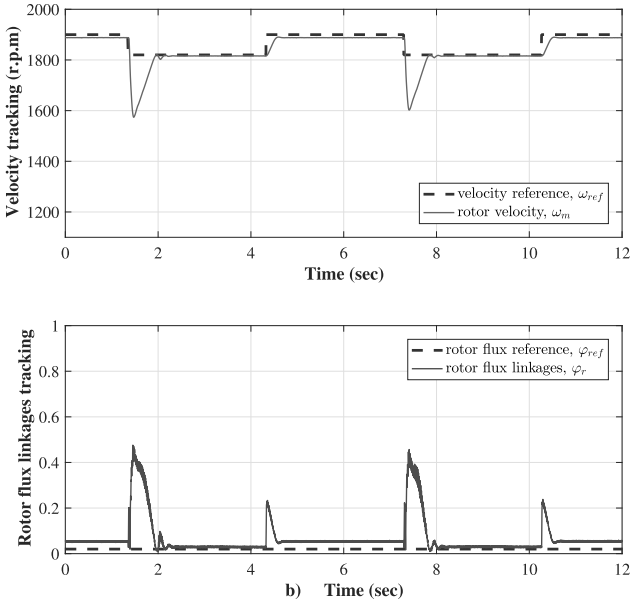

Fig. 8. Outputs tracking performance of the induction motor.

5.3. Control results of the induction motor speed

The motor velocity controller performance is pictured in Fig. 8. At high-speed reference of 1900 r.p.m., the motor achieves a speed of 1888 r.p.m. where an error of 0.63% in steady-state is presented; meanwhile, at the lower speed reference of 1820 r.p.m., the motor achieves a speed of 1816 r.p.m. where an error of 0.21% in steady-state is presented. When the speed reference falls down suddenly from 1900 r.p.m. to 1820 r.p.m, an undershoot of 187.5% appears, and the motor speed falls down to 1590 r.p.m, see Fig. 8 (a). The regulation of the rotor flux leakages squared modulus which is the second output, has a steady-state error of 30% and has a reference value of 0.02 wb^2, meanwhile, the squared modulus of rotor flux leakages has the value of 0.026 wb^2, see Fig. 8 (b).

In Fig. 9 is depicted the speed controller performance. The input $v_{\alpha s}$ (Fig. 9 (c) with a maximum value of 72 V forces the sliding variable s_α to a vicinity of the origin in finite time (Fig. 9 (b), achieving the speed tracking error ε_ω moves asymptotically to the origin (Fig. 9 (a). The steady-state speed tracking error is 1.25 rad/s and the siding surface maximum value is 0.027. The

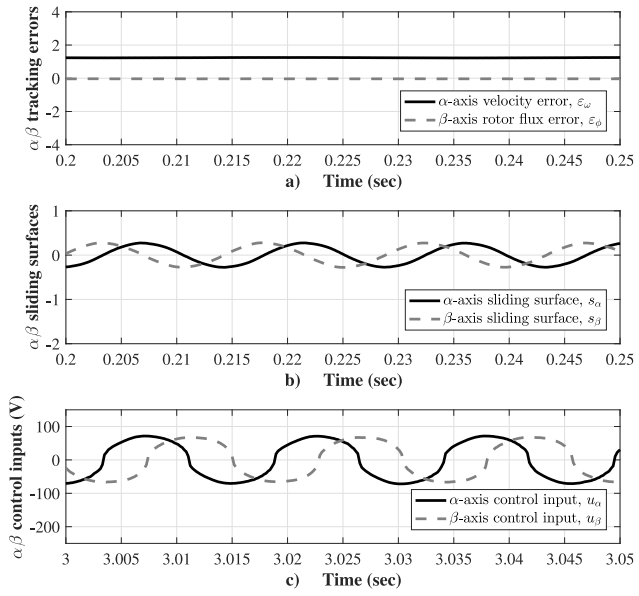

Fig. 9. Rotor speed controller performance: (a) $\alpha\beta$ tracking errors, (b) $\alpha\beta$ sliding surfaces, and (c) $\alpha\beta$ control inputs.

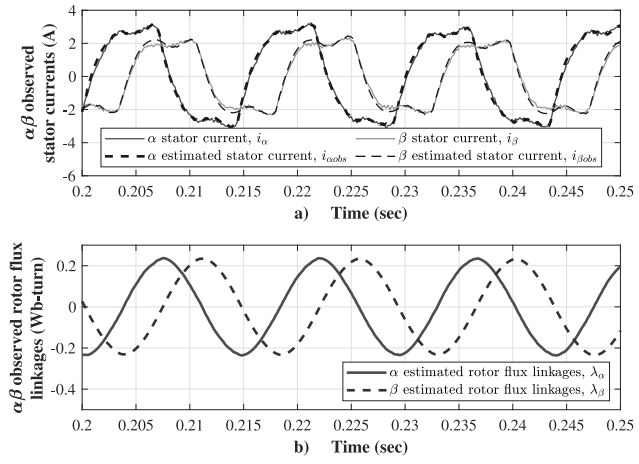

Fig. 10. Rotor flux linkages observer performance.

control input $v_{\beta s}$ (Fig. 9 (c) with a maximum value of 72 V forces the movement toward zero of the sliding surface s_β at a finite time (Fig. 9 (b), achieving that the rotor flux error ε_ϕ moves asymptotically to zero (Fig. 9 (a). The steady-state rotor flux error is - 0.03 wb^2, while the sliding variable peak value s is 0.027. The obtained results for estimating the rotor flux linkages are depicted in Fig. 10, wherein 10 (a) presents the estimation of the current $\hat{i}_{\alpha s}$ and $\hat{i}_{\beta s}$ with respect to the sensed currents $i_{\alpha s}$ and $i_{\beta s}$, where can be identified that the observed (estimated) values are very close to the measured values. Fig. 10 (b) displays the rotor linkages flux $\lambda_{\alpha r}$ and $\lambda_{\beta r}$, which have a peak value of 0.23 wb. It is important to remark that the effectiveness in tracking the stator currents by the observed currents ensures a correct estimation of the rotor winding flux linkages.

5.4. Filter-LCL characterization

The procedure for defining the three-phase LCL filter parameters is described in Section 2.3. To obtain the value of the inverter-side inductance L_r, an attenuation of 0.03 (3%) is considered in the first-order transfer function (20), where the IGBT

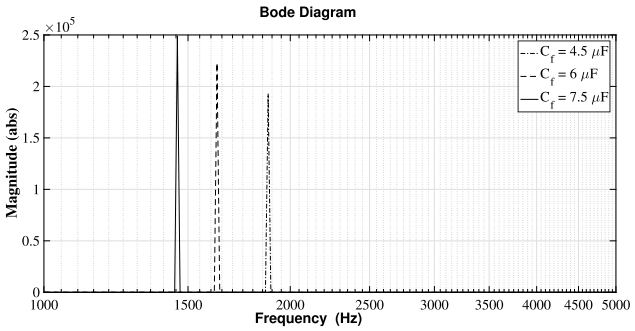

Fig. 11. Bode diagram for the resonant frequencies with C_f = 4.5, 6, and 7.5 μF.

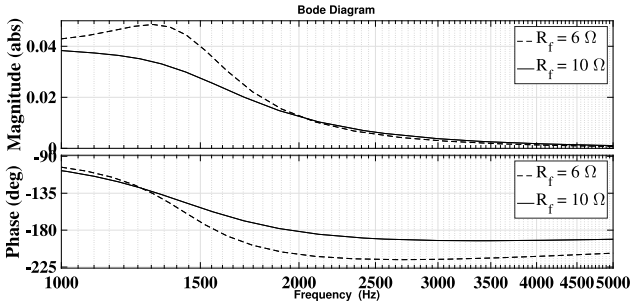

Fig. 12. Bode diagram for the frequency response with R_f = 6 and 10 Ω.

switching frequency is f_{sw} = 3.3 kHz, and then, solving for L_r from (20) results in an inductance value of L_r = 3.2 mH. Meanwhile, the grid-side inductance L_g is estimated using (21) resulting in 3.4 mH, where the switching harmonic current attenuation k_a of the LCL filter is considered of 0.02. The initial value of C_f = 4.1 μF is estimated by $C_f = 0.05C_b$ using (23) and then, this value is modified through a parametric analysis with three values of capacitance 4.5, 6, and 7.5 μF, by applying a frequency analysis in the range from 2 to 5 kHz with the transfer function of the LCL filter (26). Then, three resonant frequencies are located in the Bode diagram, as shown in Fig. 11, where the selected capacitance value is C_f = 7.5 μF that corresponds to the lowest resonant frequency of f_{res} = 1.46 kHz. Finally, the damping resistance R_f is estimated using (27), and later, this value is enhanced through a parametric analysis using the values of 6 and 10 Ω through a frequency analysis in the range from 1 to 5 kHz applying the transfer function (28). The resistance value selected is R_f = 10 Ω because it presents a lower gain at the resonant frequency of f_{res} = 1.46 kHz, as shown in the Bode diagram in Fig. 12.

6. Conclusions

A complete solution to regulate the reactive power and the induction motor speed is proposed, which is achieved through two cascade controllers applied to an AC/DC/AC power converter. The first control scheme is synthesized by using the block control linearization technique combined with the super-twisting algorithm, for regulating the reactive power and DC bus voltage, which can contribute to the power factor improvement. Specifically, the experimental results confirm the effective regulation of the reactive power and the DC-bus voltage, producing in both cases a steady-state error lower than 1%, even in presence of external disturbances produced by the active power variations, as a consequence of controlling a 3/4 HP induction motor velocity under sudden motor load changes, due to the step changes

of velocity reference. Meanwhile, the second controller is designed through the state-feedback linearization technique using the super-twisting algorithm for controlling the induction motor speed above the synchronous speed, under sudden changes in the load torque. This controller forces in finite time the sliding variable to the origin, and a posteriori, achieving an asymptotic motion to zero of the speed error. And simultaneously, the rotor flux squared modulus is regulated, where the rotor flux leakages are determined through a sliding-mode-based observer. To comply with grid interconnection standards, the three-phase LCL filter parameters are defined and experimentally validated. The cascade two controllers are validated through a laboratory test using a prototype, where the carried-out results test shows a robust operation of the proposed control scheme.

Declaration of competing interest

The authors declare that they have no known competing financial interests or personal relationships that could have appeared to influence the work reported in this paper.

References

[1] Santoyo-Anaya MA, Rodríguez-Rodríguez JR, Moreno-Goytia EL, Venegas-Rebollar V, Salgado-Herrera N. Current-sensorless VSC-pfc rectifier control with enhance response to dynamic and sag conditions using a single PI loop. IEEE Trans Power Electron 2017;33(7):6403–15.

[2] Liu J, Yin Y, Luo W, Vazquez S, Franquelo LG, Wu L. Sliding mode control of a three-phase AC/DC voltage source converter under unknown load conditions: Industry applications. IEEE Trans Syst Man Cybern 2017;48(10):1771–80.

[3] Wai RJ, Yang Y. Design of backstepping direct power control for three-phase PWM rectifier. IEEE Trans Ind Appl 2019;55(3):3160–73.

[4] Liu J, Shen X, Alcaide AM, Yin Y, Leon JI, Vazquez S, et al. Sliding mode control of grid-connected neutral-point-clamped converters via high-gain observer. IEEE Trans Ind Electron 2021;69(4):4010–21.

[5] El Fadili A, Giri F, El Magri A, Dugard L, Ouadi H. Induction motor control in presence of magnetic saturation: Speed regulation and power factor correction. In: Proceedings of the 2011 American control conference. IEEE; 2011, p. 5406–11.

[6] El Fadili A, Giri F, El Magri A, Lajouad R, Chaoui FZ. Towards a global control strategy for induction motor: Speed regulation, flux optimization and power factor correction. Int J Electr Power Energy Syst 2012;43(1):230–44.

[7] El Fadili A, Giri F, El Magri A, Lajouad R, Chaoui FZ. Adaptive control strategy with flux reference optimization for sensorless induction motors. Control Eng Pract 2014;26:91–106.

[8] Oliveira J, Araujo A, Dias S. Controlling the speed of a three-phase induction motor using a simplified indirect adaptive sliding mode scheme. Control Eng Pract 2010;18(6):577–84.

[9] Farhani F, Regaya CB, Zaafouri A, Chaari A. Real time PI-backstepping induction machine drive with efficiency optimization. ISA Trans 2017;70:348–56.

[10] Zaafouri A, Regaya CB, Azza HB, Châari A. DSP-based adaptive backstepping using the tracking errors for high-performance sensorless speed control of induction motor drive. ISA Trans 2016;60:333–47.

[11] Kundur P, Balu NJ, Lauby MG. Power system stability and control, vol. 7. McGraw-hill New York; 1994.

[12] Morfin OA, Valenzuela FA, Betancour RR, Castañeda CE, Ruíz-Cruz R, Valderrabano-Gonzalez A. Real-time SOSM super-twisting combined with block control for regulating induction motor velocity. IEEE Access 2018;6:25898–907.

[13] Chalanga A, Kamal S, Fridman LM, Bandyopadhyay B, Moreno JA. Implementation of super-twisting control: Super-twisting and higher order sliding-mode observer-based approaches. IEEE Trans Ind Electron 2016;63(6):3677–85.

[14] Wu L, Liu J, Vazquez S, Mazumder SK. Sliding mode control in power converters and drives: A review. IEEE/CAA J Autom Sin 2021;9(3):392–406.

[15] Liu J, Laghrouche S, Wack M. Observer-based higher order sliding mode control of power factor in three-phase AC/DC converter for hybrid electric vehicle applications. Internat J Control 2014;87(6):1117–30.

[16] Dávila A, Moreno JA, Fridman L. Optimal Lyapunov function selection for reaching time estimation of super twisting algorithm. In: Proceedings of the 48h IEEE conference on decision and control (CDC) held jointly with 2009 28th chinese control conference. IEEE; 2009, p. 8405–10.

[17] Liserre M, Blaabjerg F, Hansen S. Design and control of an LCL-filter-based three-phase active rectifier. IEEE Trans Ind Appl 2005;41(5):1281–91.

[18] Reznik A, Simões MG, Al-Durra A, Muyeen S. *LCL* Filter design and performance analysis for grid-interconnected systems. IEEE Trans Ind Appl 2013;50(2):1225–32.

[19] Araújo SV, Engler A, Sahan B, Antunes FLM. LCL filter design for grid-connected NPC inverters in offshore wind turbines. In: 2007 7th internatonal conference on power electronics. IEEE; 2007, p. 1133–8.

[20] Krause PC, Wasynczuk O, Sudhoff SD, Pekarek S. Analysis of electric machinery and drive systems, vol. 2. Wiley Online Library; 2002.

[21] Morfín OA, Castañeda CE, Ruiz-Cruz R, Valenzuela FA, Murillo MA, Quezada AE, et al. The squirrel-cage induction motor model and its parameter identification via steady and dynamic tests. Electr Power Compon Syst 2018;46(3):302–15.

[22] Shtessel Y, Edwards C, Fridman L, Levant A. Sliding mode control and observation. Springer; 2014.

[23] Levant A. Higher-order sliding modes, differentiation and output-feedback control. Internat J Control 2003;76(9–10):924–41.

[24] Morfin O, Aguilar B, Gabbar HA, Ornelas-Tellez F, Ruiz-Cruz R, Valderrabano-Gonzalez A, et al. Real-time induction motor velocity controller applying sosm super-twisting combined with state-feedback linearization. In: 2017 IEEE international autumn meeting on power, electronics and computing. IEEE; 2017, p. 1–6.

[25] Utkin V. Sliding mode control in mechanical systems. In: Proceedings of IECON'94-20th annual conference of IEEE industrial electronics, vol. 3. IEEE; 1994, p. 1429–31.

[26] Morfin O, Miranda U, Ruiz-Cruz R, Valenzuela F, Ornelas-Tellez F, Acosta J. State-feedback linearization using a robust differentiator combined with SOSM super-twisting for controlling the induction motor velocity. In: 2018 IEEE international autumn meeting on power, electronics and computing. IEEE; 2018, p. 1–6.